

Self-Generated Magnetic and Electric Fields at a Mach-6 Shock Front in a Low Density Helium Gas by Dual-Angle Proton Radiography

R. Hua,¹ J. Kim,¹ M. Sherlock,² M. Bailly-Grandvaux,¹ F. N. Beg,^{1,*} C. McGuffey,¹
S. Wilks,² H. Wen,³ A. Joglekar,³ W. Mori,³ and Y. Ping^{2,†}

¹Center for Energy Research, University of California, San Diego, La Jolla, California 92093, USA

²Lawrence Livermore National Laboratory, Livermore, California 94550, USA

³University of California, Los Angeles, Los Angeles, California 90095, USA



(Received 18 September 2018; revised manuscript received 17 May 2019; published 21 November 2019)

Shocks are abundant both in astrophysical and laboratory systems. While the electric fields generated at shock fronts have recently attracted great attention, the associated self-generated magnetic field is rarely studied, despite its ability to significantly affect the shock profile in the nonideal geometry where density and temperature gradients are not parallel. We report here the observation of a magnetic field at the front of a Mach ~ 6 shock propagating in a low-density helium gas system. Proton radiography from different projection angles not only confirms the magnetic field's existence, but also provides a quantitative measurement of the field strength in the range ~ 5 to 7 T. X-ray spectrometry allowed inference of the density and temperature at the shock front, constraining the plasma conditions under which the magnetic and electric fields are generated. Simulations with the particle-in-cell code LSP attribute the self-generation of the magnetic field to the Biermann battery effect ($\nabla n_e \times \nabla T_e$).

DOI: [10.1103/PhysRevLett.123.215001](https://doi.org/10.1103/PhysRevLett.123.215001)

Shocks [1] are essential components in astrophysical systems [2,3] and inertial confinement fusion (ICF) [4], especially the shock ignition configuration [5], prompting recent studies of their roles by the high energy density physics community. Despite their common occurrence, the precise shock profile—especially the associated magnetic field structure—lacks detailed investigation. Under the nonideal geometry such as the finite (albeit huge) width in astrophysics, or the nonuniform compression or heating in ICF implosions, magnetic field can become significant during the shock propagation. In recent years, as inconsistencies between experiments and radiation-hydrodynamic simulations have appeared [6,7], an appreciation of the importance of kinetic effects in shock physics [8,9] has emerged, building on earlier Vlasov-Fokker-Planck simulations [10,11] and particle-in-cell calculations [12]. Since then, the complexity of shocks has been revealed with the discovery of new effects such as electric current [13], charge separation [14], and electrodiffusion [15] at the shock front.

In recent decades, the electric fields associated with shock fronts have attracted great attention and are widely studied with proton radiography [16–20]. However, the extremely small scale of shocks and the finite resolving power of proton probing highlights the difficulty of not only differentiating between electric and magnetic fields but also of providing a quantitative description of the field structure. As a result, the critical role played by the magnetic field has been underappreciated and only the electric field has been included in experimental analysis, which has resulted in an aberration of up to a couple orders

of magnitude between experiments and simulation [16]. In addition, the numerical difficulties associated with magnetohydrodynamic simulation (MHD) of shocks imposes limitations on our ability to account for their effect on shock evolution [21]. Consequently, the magnetic fields associated with shocks remain unexplored both experimentally and theoretically.

While the existence of the magnetic field in laser target interactions has been reported [22,23], study of their evolution associated with shock propagation is rare in current literature. Recently, Rinderknecht *et al.* [24] measured the spatial profiles of the ion temperature and density in strong plasma shocks; 3D simulations predict strong magnetic fields ~ 10 to 10^2 T are present during the stagnation phase in ICF [25], which could reduce the thermal loss from the hot spot [26–28]. Improved observations are necessary for comprehensively understanding plasma shocks, as well as benchmarking codes.

In this Letter, we report the direct observation and quantitative description of a (Mach ~ 6) shock-associated magnetic field by varying the projection angle of probing protons. The experiments were conducted on the Omega-EP facility. The measurement of the self-generated electric field was reported in 2017 using the same platform but with normal incident protons to the apex of the shock front [20]. The explanation that a magnetic field was diagnosed in the current Letter using oblique incident protons whereas an electric field was probed in the previous paper by normal incident protons is discussed in detail in the Supplemental Material, Sec. I [29].

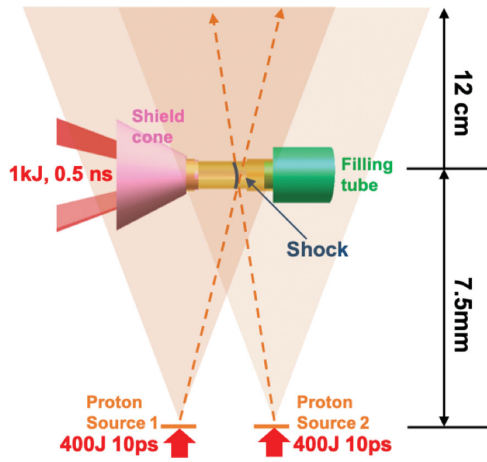


FIG. 1. (a) Schematic diagram of the experimental setup. Proton source 1 is located $\sim 800 \mu\text{m}$ behind the shock longitudinally and 1 mm away from proton source 2 that is $\sim 200 \mu\text{m}$ in front.

The main target is a cylindrical tube 2 mm wide and 5 mm long, filled with pure helium gas at 1 atm. The tube is made of $50 \mu\text{m}$ polystyrene (CH) with three $1 \mu\text{m}$ -thick windows, two for proton radiograph and one for soft x-ray spectroscopy. A strong shock was created when two synchronized long pulse laser beams delivered 1 kJ total energy in 0.5 ns square pulses with $750 \mu\text{m}$ spot size to ablate a $2 \mu\text{m}$ SiO_2 foil located on one end of the tube [30]. The shock velocity is $\sim 600 \text{ km/s}$. The calculation of the Mach number as the ratio of shock velocity to the sound speed of the rest medium took into account the preheat ahead of the shock front, as observed from the x-ray spectra shown in the Supplemental Material, Sec. III [29].

The probing protons, spanning 20 MeV [31] in energy, were produced by a short pulse laser (400 J, 10 ps) interacting with a $40 \mu\text{m}$ copper strip. This proton side-lighter target was positioned 7.5 mm laterally from the tube axis and the RCF

stack was opposite it 12 cm from the tube axis, corresponding to a magnification of $17\times$. Two such proton sources were located 1 mm apart as labeled in Fig. 1: “proton source 1” was located $800 \mu\text{m} \pm 7.5 \mu\text{m}$ behind the shock front along the tube axis and “proton source 2” was located $200 \mu\text{m} \pm 7.5 \mu\text{m}$ ahead [32]. Protons from the two sources probed the shock at two different lines of sight. A semicircular copper grid with $55 \mu\text{m}$ bar and $340 \mu\text{m}$ gap size was attached to the bottom of the tube as a spatial reference.

Figures 2(a) and 2(b) show the RCF images of two identical shocks probed from proton sources 1 and 2, where the color scale represents the dose per pixel in Gy unit (J/kg). The white arrow on each image identifies the shock front positions 3 ns after the shock creation. We analyzed each shot through the RCF stack, observing an energy-dependent change of the ring structure over 9 to 16 MeV. Because the resolving power is better at higher proton energy, we focus our analysis on the image produced by 15.6 MeV protons, due to their superior contrast. Analysis on radiography data from lower energy protons provided similar results as shown in the Supplemental Material, Sec. V [29].

The contrary proton flux pattern in Fig. 2(a), a higher flux (bright ring) ahead, and 2(b), a lower flux (dark ring) ahead, allows us to conclude that the field at the shock front deflects protons in a manner dependent on their incident angles. This signature confirms the domination of magnetic field over electric field, since electric fields deflect charged particles independently of their incident angles. Figure 3 displays the detailed process of how a magnetic field at the shock front deflects protons. Given the azimuthal symmetry of the system, the field points out of the paper at the bottom part of the shell (nearer the proton source) and points into the paper at the top part (farther from the proton source). Figure 3(a) shows the proton trajectories intersecting with the shell twice at both the near and far parts.

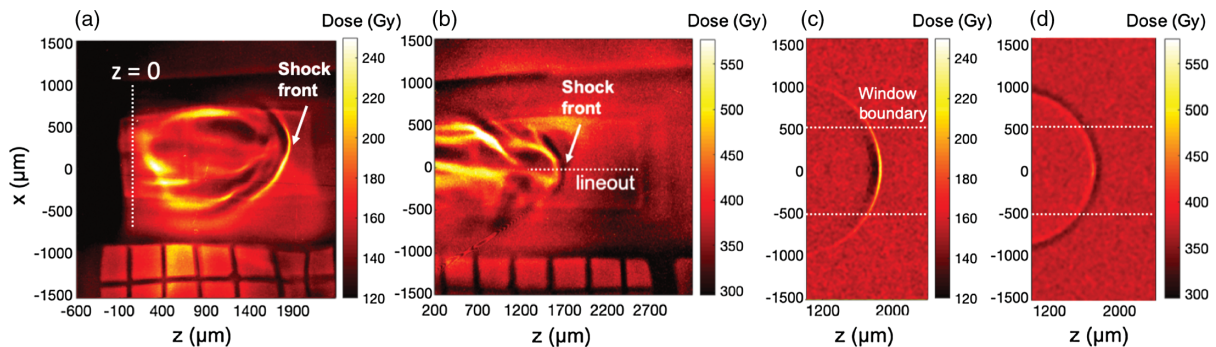


FIG. 2. RCF image from proton source 1 by (a) and proton source 2 location by (b). The windows are, respectively, ~ 2 and ~ 2.5 mm long along the z axis. Because the film was ~ 5 cm square, which corresponded to $\sim 3000 \mu\text{m}$ at the target plane, its edges provided sharp limits to the field of view. In (b), the left edge of the window was not captured due to the limited field of view. Shocks were initiated at location 0 along the z axis by the ablation of a SiO_2 foil. The images were captured 3 ns after the shock initiation by 15.6 MeV protons. Values in the color bar represent doses in Gy units (J/kg). The two shocks are of identical conditions, only the proton source location varied. (c),(d) Simulated images from proton source 1 and 2 produced by a 3D particle tracking code. The white dashed lines indicate the corresponding window boundaries’ position.

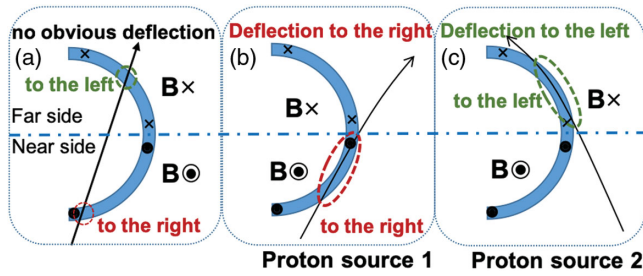


FIG. 3. Cross sectional top view of the hemispherical shell model of the shock front B field. (a) The case where a proton intersects the shell twice, resulting in deflections right then left located at the red and green dashed circles, respectively. Because the deflections are opposing, no obvious variation can be observed on the film. (b) and (c) The cases where a proton intersects only the near or far side of the shell, respectively. The figure conveys the idea of right deflection and left deflection, qualitatively, and the incident angles of the proton trajectories are not drawn to scale.

Figures 3(b) and 3(c) show the protons interacting mostly on the near or far side of the shell, respectively. For the (a) case, regardless of the source location, deflections by the two intersections cancel each other, thus unbending the final proton trajectories. For the (b) and (c) cases, where a proton grazes mostly the near or far part of the shell, the signal from source 1 and 2 will be deflected in opposite directions. Consequently, protons from source 1 are deflected to the right given the out-of-paper B pointing and produce the bright leading ring as observed in Fig. 2(a), while protons from source position 2 are deflected to the left and result in the dark leading ring as shown by Fig. 2(b). When it comes to the electric field, protons are deflected to the right regardless of their incident angles due to the radially outward directionality of the field [20].

Despite the fact that both field types must exist simultaneously at the shock front, we will show later that the magnetic field dominates and the contribution from electric field is ignorable under our experimental conditions. It is also found that the effect of density scattering, which could

also cause proton deflection due to the sharp density gradient at the shock front, is negligible under our condition as discussed in detail in the Supplemental Material, Sec. II [29], which includes Refs. [33,34].

We employed a 3D particle tracking program to simulate the proton probing scheme and study the field structure by quantitatively matching the experimental data with simulation results. The geometric diagram in the simulation replicates the proton probing setup. At the shock region, an azimuthal magnetic field is implemented given the cylindrical symmetry of the shock. The 3D field has nonzero magnitude only within a hemispherical shell of 1 mm radius and its direction points clockwise as viewed from the apex. The Leapfrog method [35] was used to compute the proton trajectories as they experience the Lorentz force in the prescribed fields. By adjusting the field parameters magnetic strength, shell thickness, and its spatial distribution along both x and z axes, we are able to quantitatively fit the experimental data.

To take into account both magnetic and electric fields in our 3D simulations, an electric field corresponding to a 300 V potential and varied width is included. The electric potential was obtained from another diagnostic, a 1D resolved soft x-ray spectrometer, known as a VSG (variable line spaced grating spectrometer) [36], which measured the shock temperature and density to be ~ 140 eV and ~ 1.5 mg/cm³ (see the Supplemental Material, Sec. III [29], which includes Ref. [37]). According to the expression $\Delta\Phi \approx \ln(\rho_2/\rho_1)k_B T_e/e$, the electric field potential is ~ 300 V based on the shock front condition. In contrast to previous work [16] which only considered the effect of the electric field on the proton trajectories due to normal incidence, we found that the electric field's contribution is always negligible in comparison to the experimental data when varying the simulated width from a few to hundreds of μm . The 30 μm case is shown in Fig. 4. It is clear that magnetic field dominates the deflection.

Figures 2(c) and 2(d) show the simulated results by 15.6 MeV protons from source 1 and 2, respectively. These images qualitatively reproduced a proton flux pattern from

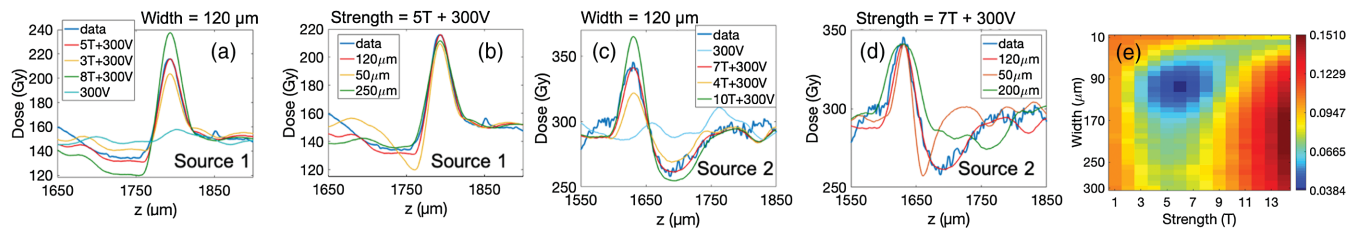


FIG. 4. Lineouts from the center axis of the proton rings both from experimental and simulated data. First row of the plots show fittings for the proton source 1 image and the second row for proton source 2. On each plot, the dark blue curve represents the data and the red curve is best fitting. The two additional curves show the misfit when a certain parameter deviates from its best-fit value: (a) and (c) The deviation of magnetic strength. The spatial profile is fixed triangular and the field thickness is 120 μm ; (b) and (d) the deviation of the shell thickness. The spatial profile is fixed as triangular and the peak magnetic strengths are at 5 and 7 T, respectively. The light blue curve on (a) and (c) plot the results from pure electric field of 300 V potential, which is negligible compared to the measurement. (e) The fitting error map. Blue indicates smaller error, better fitting and red indicates larger error, worse fitting.

each proton source. To make quantitative comparison with the experimental data, the field width was scanned from zero to the millimeter scale, the field strength from zero to hundreds of T, and the field spatial profile along the z axis was varied from uniform distribution (square) to triangular distribution until the best match was found. The spatial profile along the shell is assumed to be uniform in the calculation. The raw simulated images were convolved with the experimental spatial resolution $\sim 25 \mu\text{m}$.

Figure 4 shows the fitting processes for magnetic strength and the field width. Details on the spatial profiles of the fields are provided in Sec. IV in the Supplemental Material [29]. The experimental and simulated transverse dose lineouts are taken from the center axes (position at $x = 0$) of the rings as indicated by the horizontal white dashed line in Fig. 2(b). Our best fit to the data indicates the magnetic field is well represented by a triangular shaped spatial profile that spans over $120 \mu\text{m}$ within the shell with a peak amplitude of 5 and 7 T, respectively, for the proton source 1 and 2. Figures 4(a) and 4(b) show the fits corresponding to proton source 1, and (4c), 4(d) show those from 2. On each plot, the dark blue curve represents the experimental data and the red curve displays the best fit. Two additional curves show the sensitivity by varying one parameter. For example, in Fig. 4(a) we fixed the field width at $120 \mu\text{m}$ then varied the peak amplitude. The simulated curves noticeably differ from the experimental curves when the field strength deviates from 5 T to either 3 or 8 T. Similarly, Fig. 4(b) displays the fitting sensitivity to the field width.

To confirm the magnetic field extracted by forward fitting the experimental data, a thorough scan for the field amplitude from 1 to 14 T and width from 10 to $300 \mu\text{m}$ was performed and the result is displayed by Fig. 4(e). The fitting error from 1600 to $1850 \mu\text{m}$ along the z axis is calculated as $\sqrt{(1/n)\sum((D_i - S_i)^2/D_i^2)}$, where D_i represents the data, S_i is from the simulated image, and n is the number of the sampled points. The region at $z < 1600 \mu\text{m}$ is the ablator area behind the shock which displays complex 3D structure and is not included in our simple model of the magnetic field at the shock front. Figure 4(e) shows the average of four error maps including the two radiographs of 15.6 MeV protons for both sources discussed in the Letter and the other two of lower proton energies, 11.2 MeV from source 1 and 9.5 MeV from source 2. The amplitude and width of the magnetic field determined by the four radiographs converges to $6 \pm 1 \text{ T}$, $110 \pm 20 \mu\text{m}$ to fit the data within 5%. Each of the individual fitting error maps and more discussion on the error analysis are provided in the Supplemental Material, Sec. VI [29].

Generation of the discussed magnetic field is attributed to the Biermann battery effect ($\nabla n_e \times \nabla T_e$). The ablator is $\sim 1.9 \text{ mm}$ in diameter, the central $\sim 750 \mu\text{m}$ of which was pushed into the gas at a high velocity by laser ablation. The density evolution, determined by advection and the

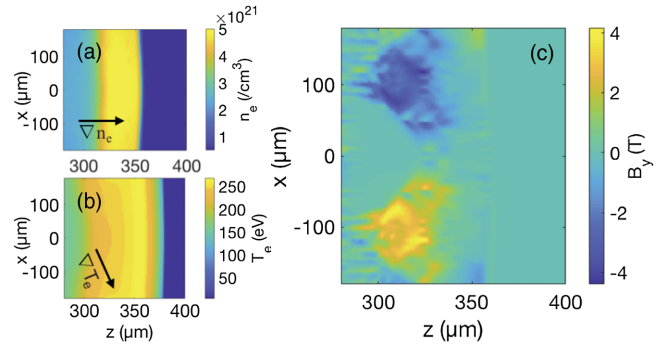


FIG. 5. (a) and (b) Density and temperature map from the PIC simulation by LSP at 300 ps. (c) Simulated azimuthal magnetic field structure at 300 ps.

temperature evolution, determined by thermal diffusion, obey different physical processes and therefore eventually evolve into different spatial distributions during the shock propagation. To further investigate the field evolution, we simulated the shock propagation using the particle-in-cell code LSP [38] with an implicit, hybrid method [12]. The initial density and temperature conditions are taken from the VSG measurement at 2.6 ns and the initial density variation along the x axis calculated by the radiation-hydrodynamic code FLASH [39] was applied. In the simulation, a hot-dense plasma— n_e of $2.4 \times 10^{21} \text{ cm}^{-3}$ (Gaussian profile in the transverse direction) and T_e of 150 eV—moves toward a uniform low-density plasma— n_e of $0.34 \times 10^{21} \text{ cm}^{-3}$ and T_e of 10 eV—with a velocity of 600 km/s. The simulation box is $400 \times 400 \mu\text{m}$, smaller compared to the target size due to the consideration of computational expense. The central part of the compressed region penetrates further into the low-density plasma due to its higher initial density, resulting in a slight bulge at the shock front as shown by Fig. 5(a). The temperature contour becomes curved as the shock propagating, thus resulting in a transverse gradient as displayed by the arrow on Fig. 5(b). According to the Biermann battery effect [40], nonparallel density and temperature gradients drive an azimuthal magnetic field, shown in Fig. 5(c). The peak value reaches more than 4 T in the simulation at 200 ps and is sustained until 300 ps, when the simulation ended. The magnitude of the magnetic field fluctuates within $\sim 15\%$ when the heat flux limiter varies from 0.1 to 0.8. In addition, the shock driven electric potential reaches $\sim 500 \text{ V}$ in the simulation, which is the same order of magnitude as the experimentally derived estimate shown above.

In summary, we have observed the magnetic field associated with a Mach ~ 6 shock front and characterized its structure by varying the incident angle of probing protons. Quantitative analysis indicates the field profile $6 \pm 1 \text{ T}$ with a characteristic width of $110 \pm 20 \mu\text{m}$. The density and temperature at the shock front measured by soft x-ray spectroscopy constrain the electric potential to be 300 V. Contrary to the common interpretation that proton

deflectometry is mainly caused by electric field, we find that the effect of the magnetic component of the Lorentz force dominates the signal. Further investigation with PIC simulations indicates that the field is mostly generated by the Biermann battery mechanism.

The author would like to thank Russel Wallace and the team at General Atomics for their excellent work on target fabrication, and the OMEGA-EP team for outstanding experimental support. This work was performed under DOE Contract No. DE-AC52-07NA27344 with support from OFES Early Career program and LLNL LDRD program. C.M. is supported by the FES High Energy Density Laboratory Plasmas program (DE-SC0014600). The work has been partially supported by the University of California Office of the President Lab Fee Grant No. LFR-17-449059.

*fbeg@eng.ucsd.edu

†ping2@llnl.gov

- [1] M. Y. Jaffrin and R. F. Probstein, *Phys. Fluids* **7**, 1658 (1964).
- [2] G. Gregori, B. Reville, and F. Miniati, *Phys. Rep.* **601**, 1 (2015).
- [3] J. Meinecke, H. Doyle, F. Miniati, A. Bell, R. Bingham, R. Crowston, R. Drake, M. Fatenejad, M. Koenig, Y. Kuramitsu *et al.*, *Nat. Phys.* **10**, 520 (2014).
- [4] S. Atzeni, J. Meyer-Ter-Vehn, and J. Meyer-ter Vehn, *The Physics of Inertial Fusion* (Clarendon Press, Oxford, 2004), Vol. 125.
- [5] R. Betti, C. Zhou, K. Anderson, L. Perkins, W. Theobald, and A. Solodov, *Phys. Rev. Lett.* **98**, 155001 (2007).
- [6] H. Herrmann, J. Langenbrunner, J. Mack, J. Cooley, D. Wilson, S. Evans, T. Sedillo, G. Kyrala, S. Caldwell, C. Young *et al.*, *Phys. Plasmas* **16**, 056312 (2009).
- [7] H. G. Rinderknecht, M. Rosenberg, C. Li, N. Hoffman, G. Kagan, A. Zylstra, H. Sio, J. Frenje, M. G. Johnson, F. Séguin *et al.*, *Phys. Rev. Lett.* **114**, 025001 (2015).
- [8] M. Rosenberg, H. Rinderknecht, N. Hoffman, P. Amendt, S. Atzeni, A. Zylstra, C. Li, F. Séguin, H. Sio, M. G. Johnson *et al.*, *Phys. Rev. Lett.* **112**, 185001 (2014).
- [9] B. D. Keenan, A. N. Simakov, L. Chacón, and W. T. Taitano, *Phys. Rev. E* **96**, 053203 (2017).
- [10] M. Casanova, O. Larroche, and J.-P. Matte, *Phys. Rev. Lett.* **67**, 2143 (1991).
- [11] F. Vidal, J. Matte, M. Casanova, and O. Larroche, *Phys. Fluids B* **5**, 3182 (1993).
- [12] C. Bellei, H. Rinderknecht, A. Zylstra, M. Rosenberg, H. Sio, C. Li, R. Petrasso, S. Wilks, and P. Amendt, *Phys. Plasmas* **21**, 056310 (2014).
- [13] H. Yemin and H. Xiwei, *Phys. Plasmas* **10**, 2704 (2003).
- [14] P. Amendt, O. Landen, H. Robey, C. Li, and R. Petrasso, *Phys. Rev. Lett.* **105**, 115005 (2010).
- [15] G. Kagan and X.-Z. Tang, *Phys. Plasmas* **19**, 082709 (2012).
- [16] C. Li, F. Séguin, J. Rygg, J. Frenje, M. Manuel, R. Petrasso, R. Betti, J. Delettrez, J. Knauer, F. Marshall *et al.*, *Phys. Rev. Lett.* **100**, 225001 (2008).
- [17] T. Morita, N. Kugland, W. Wan, R. Crowston, R. Drake, F. Fiúza, G. Gregori, C. Huntington, T. Ishikawa, M. Koenig *et al.*, *J. Phys. Conf. Ser.* **688**, 012071 (2016).
- [18] H.-S. Park, C. Huntington, F. Fiúza, R. Drake, D. Froula, G. Gregori, M. Koenig, N. Kugland, C. Kuranz, D. Lamb *et al.*, *Phys. Plasmas* **22**, 056311 (2015).
- [19] J. Rygg, F. Séguin, C. Li, J. Frenje, M.-E. Manuel, R. Petrasso, R. Betti, J. Delettrez, O. Gotchev, J. Knauer *et al.*, *Science* **319**, 1223 (2008).
- [20] R. Hua, H. Sio, S. Wilks, F. Beg, C. McGuffey, M. Bailly-Grandvaux, G. Collins, and Y. Ping, *Appl. Phys. Lett.* **111**, 034102 (2017).
- [21] C. Graziani, P. Tzeferacos, D. Lee, D. Q. Lamb, K. Weide, M. Fatenejad, and J. Miller, *Astrophys. J.* **802**, 43 (2015).
- [22] L. Gao, P. Nilson, I. Igumenshchev, M. Haines, D. Froula, R. Betti, and D. Meyerhofer, *Phys. Rev. Lett.* **114**, 215003 (2015).
- [23] L. Willingale, P. Nilson, M. Kaluza, A. Dangor, R. Evans, P. Fernandes, M. Haines, C. Kamperidis, R. Kingham, C. Ridgers *et al.*, *Phys. Plasmas* **17**, 043104 (2010).
- [24] H. G. Rinderknecht, H.-S. Park, J. Ross, P. Amendt, D. Higginson, S. Wilks, D. Haberberger, J. Katz, D. Froula, N. Hoffman *et al.*, *Phys. Rev. Lett.* **120**, 095001 (2018).
- [25] C. Walsh, J. Chittenden, K. McGlinchey, N. Niasse, and B. Appelbe, *Phys. Rev. Lett.* **118**, 155001 (2017).
- [26] P. Chang, G. Fiksel, M. Hohenberger, J. Knauer, R. Betti, F. Marshall, D. Meyerhofer, F. Séguin, and R. Petrasso, *Phys. Rev. Lett.* **107**, 035006 (2011).
- [27] S. A. Slutz and R. A. Vesey, *Phys. Rev. Lett.* **108**, 025003 (2012).
- [28] P. Schmit, P. Knapp, S. Hansen, M. Gomez, K. Hahn, D. Sinars, K. Peterson, S. Slutz, A. Sefkow, T. Awe *et al.*, *Phys. Rev. Lett.* **113**, 155004 (2014).
- [29] See Supplemental Material at <http://link.aps.org/supplemental/10.1103/PhysRevLett.123.215001> for the measurement of temperature and density at the shock front by an x-ray spectrometer.
- [30] H. Sio, R. Hua, Y. Ping, C. McGuffey, F. Beg, R. Heeter, C. Li, R. Petrasso, and G. Collins, *Rev. Sci. Instrum.* **88**, 013503 (2017).
- [31] S. Wilks, A. Langdon, T. Cowan, M. Roth, M. Singh, S. Hatchett, M. Key, D. Pennington, A. MacKinnon, and R. Snavely, *Phys. Plasmas* **8**, 542 (2001).
- [32] F. Marshall, R. Craxton, M. Bonino, R. Epstein, V. Y. Glebov, D. Jacobs-Perkins, J. Knauer, J. Marozas, P. McKenty, S. Noyes *et al.*, *J. Phys. (Paris)* **133**, 153 (2006).
- [33] V. L. Highland, *Nucl. Instrum. Methods* **129**, 497 (1975).
- [34] A. Dubey, K. Antypas, M. K. Ganapathy, L. B. Reid, K. Riley, D. Sheeler, A. Siegel, and K. Weide, *Parallel Comput.* **35**, 512 (2009).
- [35] C. K. Birdsall and A. B. Langdon, *Plasma Physics via Computer Simulation* (Taylor & Francis Group, New York, 2004).
- [36] J. Park, G. Brown, M. Schneider, H. Baldis, P. Beiersdorfer, K. Cone, R. Kelley, C. Kilbourne, E. Magee, M. May *et al.*, *Rev. Sci. Instrum.* **81**, 10E319 (2010).
- [37] J. Macfarlane, I. Golovkin, P. Woodruff, and P. Wang, 34th Meeting of the American Physical Society (APS) Division

- of Atomic, Molecular and Optical Physics, 2003, Boulder, Colorado (2003), DAMOP03, abstract id. J1.181.
- [38] D.R. Welch, D. Rose, B. Oliver, and R. Clark, *Nucl. Instrum. Methods Phys. Res., Sect. A*, **464**, 134 (2001).
- [39] B. Fryxell, K. Olson, P. Ricker, F. Timmes, M. Zingale, D. Lamb, P. MacNeice, R. Rosner, J. Truran, and H. Tufo, *Astrophys. J. Suppl. Ser.* **131**, 273 (2000).
- [40] L. Biermann, *Z. Naturforsch.* **5A**, 65 (1950).